

# Structure of Transmembrane Helix 8 and Possible Membrane Defects in CFTR

Valentina Corradi,<sup>1</sup> Ruo-Xu Gu,<sup>1</sup> Paola Vergani,<sup>2</sup> and D. Peter Tieleman<sup>1,\*</sup>

<sup>1</sup>Centre for Molecular Simulation and Department of Biological Sciences, University of Calgary, Calgary, Alberta, Canada and <sup>2</sup>Research Department of Neuroscience, Physiology and Pharmacology, University College London, London, United Kingdom

**ABSTRACT** The cystic fibrosis transmembrane conductance regulator (CFTR) is an ion channel that regulates the flow of anions across epithelia. Mutations in CFTR cause cystic fibrosis. CFTR belongs to the ATP-binding cassette transporter superfamily, and gating is controlled by phosphorylation and ATP binding and hydrolysis. Recently obtained ATP-free and ATP-bound structures of zebrafish CFTR revealed an unwound segment of transmembrane helix (TM) 8, which appears to be a unique feature of CFTR not present in other ATP-binding cassette transporter structures. Here, using  $\mu$ s-long molecular dynamics simulations, we investigate the interactions formed by this TM8 segment with nearby helices in both ATP-free and ATP-bound states. We highlight ATP-dependent interactions as well as the structural role of TM8 in maintaining the functional architecture of the pore via interactions common to both the ATP-bound and ATP-free state. The results of the molecular dynamics simulations are discussed in the context of the gating mechanism of CFTR.

The cystic fibrosis transmembrane conductance regulator (CFTR) regulates anion flow through the apical membrane of epithelia (1). Defects in CFTR cause cystic fibrosis, a disease in which the movement of ions and water across epithelia is compromised, allowing for thick secretions to accumulate mainly in the airways, digestive, and reproductive systems (2). CFTR, although a member of the ATP-binding cassette transporter superfamily, functions as a channel, switching between closed and open states (3).

An interesting feature of several recently obtained CFTR structures is a region of transmembrane helix (TM) 8 that is partially unwound (residues 929–938 in zebrafish CFTR (zCFTR), corresponding to residues 921–930 in human CFTR (hCFTR)), thus breaking the  $\alpha$ -helical structure (4–6). This feature, common to the ATP-free and ATP-bound states, might underlie CFTR's unique channel function (6). To investigate the interactions between this segment and nearby helices and how this segment can be partially unwound despite being in the membrane, we embedded the structure of zCFTR in the ATP-free and ATP-bound state in a 1-palmitoyl-2-oleoyl-sn-glycero-3-phosphocholine lipid bilayer. We performed atomistic molecular dynamics simulations for a total of 3 and 1.5  $\mu$ s of simulation time for the ATP-free and ATP-bound systems, respectively (Fig. 1; Table S1).

The conformation of individual domains (transmembrane domains (TMDs) and nucleotide binding domains (NBDs)), based on root mean-square deviation, interdomain distances, and secondary structure analyses, remains stable over the simulations (Figs. S1–S4). In the ATP-free system, we noticed a closing motion of the NBDs, as has also been reported by others (7) (Fig. S1).

The unwound segment of TM8 remains stable during all the simulations in both systems (Figs. S3 and S4). The extracellular end of TM8, because of its different orientations in the ATP-free and the ATP-bound states (6), can establish interactions with residues of TM6 only in the presence of ATP (Y925-S342 (TM6)) (Fig. 2, A and C). If the hydrogen-bond interaction between this residue pair is not present in the ATP-bound state (Fig. 2 C), the distance between the  $\alpha$ -carbons is not significantly increased (Fig. S5 A), with no noteworthy opening of the pore and the side chain of Y925 still facing the central pore (Fig. S5 B). The interaction between Y927 and S875 (TM8) is also detected only in the ATP-bound state (Fig. 2 C). Further along TM8, we identify several residues that interact with nearby helices in both states, i.e., the E932-R348 (TM6), S933-F312 (TM5), M937-Y305 (TM5), M937-Q1004 (TM9), and R941-E871 (TM7) pairs (Fig. S6). The ATP-free state of the hCFTR structure (4) adopts the same conformation as the ATP-free zebrafish one (5), and the residue pairs here analyzed for the zCFTR are conserved in hCFTR (Fig. 2 D; Table S2).

The unfolded segment of TM8 exposes the backbone and side chain of residues 930–941 to the hydrophobic region of

Submitted November 14, 2017, and accepted for publication March 5, 2018.

\*Correspondence: [tieleman@ucalgary.ca](mailto:tieleman@ucalgary.ca)

Editor: Jose Faraldo-Gomez.

<https://doi.org/10.1016/j.bpj.2018.03.003>

© 2018 Biophysical Society.

This is an open access article under the CC BY-NC-ND license (<http://creativecommons.org/licenses/by-nc-nd/4.0/>).



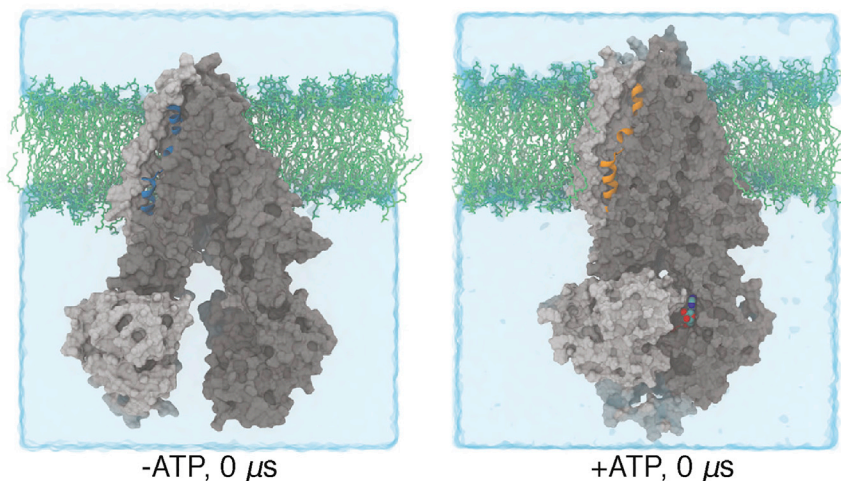


**FIGURE 1** Simulation setup. The ATP-free ( $-ATP$ , *left*) and ATP-bound ( $+ATP$ , *right*) zCFTR structures were embedded in a 1-palmitoyl-2-oleoyl-sn-glycero-3-phosphocholine bilayer (*light green sticks*). TMD1-NBD1 and TMD2-NBD2 are shown in dark and light surfaces, respectively. TM8 is highlighted in blue and orange cartoons for the two systems. Water (*light cyan surface*) and lipids are clipped for clarity.

the lipid bilayer, with the side chain of R941 reaching E871 (TM7) to establish salt-bridge interactions (Fig. 2, *A*, *E*, and *F*). In the ATP-free state, we observed simulations in which the salt bridge between these two residues is missing, leading to the penetration of water and lipid headgroups inside the membrane and the formation of a clear water channel (Fig. 2 *E*; Fig. S7). This membrane defect, once established, remains stable for the duration of the simulation. Water molecules from the main cavity of the channel can also contribute to the pool of water molecules. In the absence of the defect, water molecules from the inner cavity of CFTR can reach this region of TM8 to interact with E871 and R941. Y927 participates in these interactions only in the ATP-free state (Fig. 2, *E–G*).

In all other ATP-binding cassette exporter structures, the TMs are organized in a roughly symmetrical pattern with no breaks in their helical structure (8). The unwound segment of TM8 is then a unique feature of CFTR (4–6) that suggests a solution for a long-standing puzzle: why are the transmembrane helices known to line the permeation pathway not symmetrically distributed between TMD1 and TMD2? In particular, cysteine-accessibility studies performed on TM7 and TM1 gave very different results (9–11), indicating that the latter, but not the former, formed part of the permeation pathway (12,13). Chen and colleagues (4–6) discovered that the unwound portion of TM8 and the resulting bend position the extracellular end of TM8 closer to the permeation pathway. This displaces TM7 further from the protein's central axis, thus explaining the lack of contribution of TM7 to the anion permeation pathway.

Contacts between TM8 and TM6 are known to be required for maintaining the functional architecture of the channel, as in the case of residues E932 and R348 (14,15), the interaction of which is retrieved in both ATP-bound and ATP-free simulation systems (Fig. S6). TM8 also interacts with TM5, from the intracellular side to the kink at F312, allowing dynamic interactions that stabilize the unwound segment of TM8 in both simulation systems. Overall,

although not many of the residues that form molecular contacts with the unwound stretch of TM8 have been studied functionally, the network of molecular contacts between TM8 and the nearby helices investigated in our simulations can explain the stability of the unwound segment in both the ATP-free and the ATP-bound state and is consistent with an active role of TM8 in the functional structure of the channel.

However, the current ATP-bound structure is not a fully open channel, and the protrusion of TM8 residues toward the central pore interferes with anion flow, confirmed by the fact that an interaction is formed between TM8 and TM6, located in the narrowest portion of the pore (3,16). Thus, within the gating cycle of CFTR, the ATP-dependent interaction between the N-terminal of TM8 and TM6 might be transient as part of an intermediate state that provides an additional gate preventing anion flow through the channel. Although ATP binding and NBD dimerization are coupled with the channel entering the “open burst” state (17), “flicker” closures of the pore occur within the open burst with timescales that are not consistent with ATP hydrolysis (18–20). As suggested by Zhang and colleagues (6), the ATP-bound cryo-electron microscopy structure might have captured a flicker-closed state artifactually stabilized by experimental conditions. The alternative hypothesis proposed by these authors, that the extracellular TM8 (and TM12) might reorientate within microseconds to a position allowing fast anion flow, seems unlikely, given the relatively stable position of these secondary structure elements and the lack of a major opening of the pore between TM8 and TM6.

Two of the ATP-free, inward-facing simulations showed an unusual lipid organization near TM8. A strong membrane defect forms near R941 and E871, whereas no lipid headgroups were found in the proximity of these residues in the remaining three ATP-free simulations or in the two ATP-bound ones. Although the presence of charged residues buried along TM helices is not common, there are examples in which such residues play important biological roles, for instance, in integrin receptors (21). The presence of a

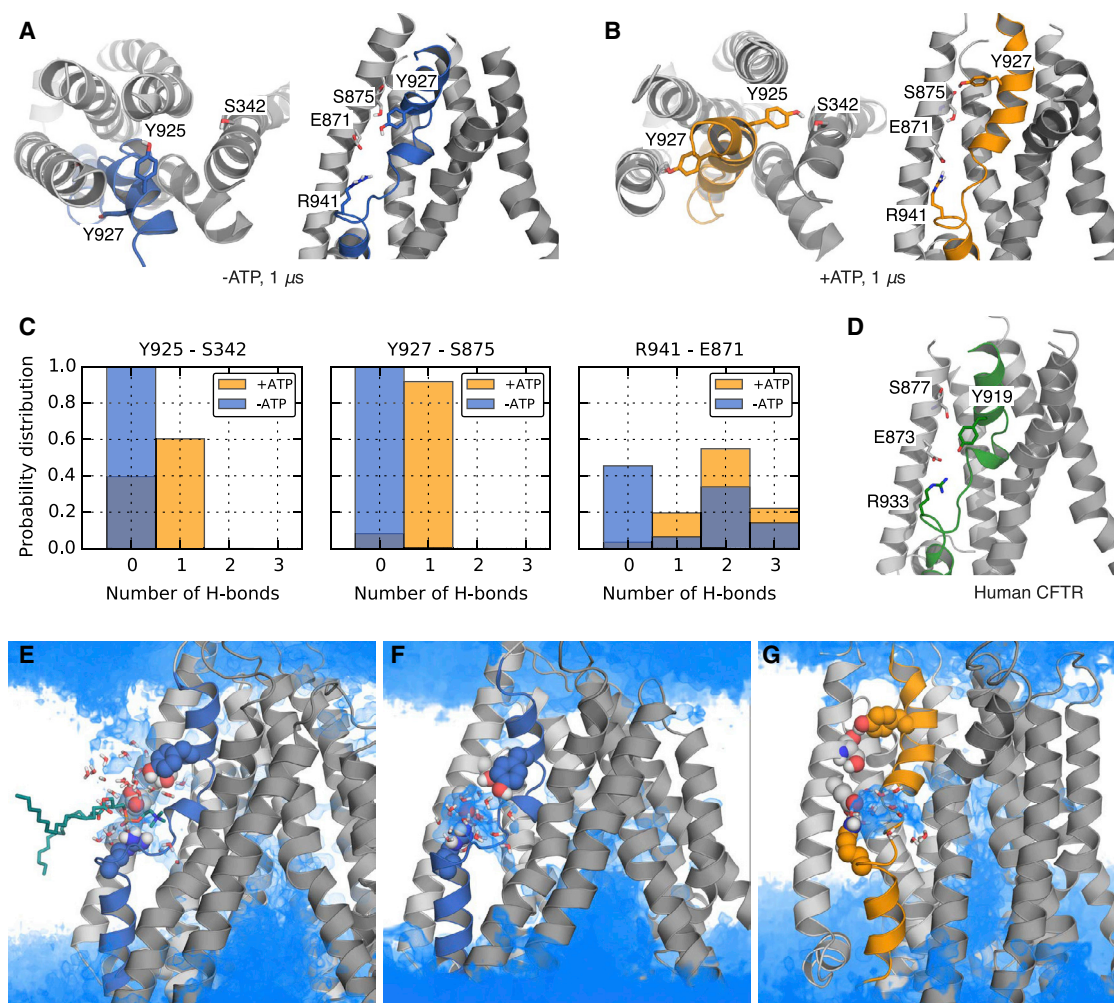


**FIGURE 2** TM8 orientation and selected interactions. (**A** and **B**) Extracellular and side views of TM8 and neighboring helices in the ATP-free ( $-$ ATP) and ATP-bound ( $+$ ATP) system after 1  $\mu$ s of simulation time are shown. The side chains of residues Y925, S342, Y927, S875, R941, and E871 are shown as sticks. TMD1 and TMD2 are shown in dark and light gray cartoons, respectively, with TM8 highlighted in blue ( $-$ ATP) and orange ( $+$ ATP) cartoons. (**C**) The probability distribution of the number of hydrogen bonds detected between the selected residue pairs is shown in blue for the ATP-free simulations ( $-$ ATP) and in orange for the ATP-bound ( $+$ ATP) simulations. (**D**) Side view of TM8 (green) in the ATP-free, hCFTR structure (Protein Data Bank: 5UAK). The residues corresponding to the zebrafish residues shown in panels (**A**–**C**) are shown as sticks. (**E**–**G**) The number density of water molecules, calculated during the last 50 ns of the simulation, is shown as a blue volume map and overlapped to the last frame of (**E**) the 1- $\mu$ s-long ATP-free simulation, showing the membrane defect; (**F**) run 3 of the ATP-free, 500-ns-long simulation, with no membrane defect; and (**G**) the 1- $\mu$ s-long ATP-bound simulation, with no membrane defect. The protein is represented as in panels (**A** and **B**). The side chains of Y927, S875, E871, and R941 are shown as spheres, and the nearby water molecules within an 8- $\text{\AA}$  cutoff from R941 and E871 are shown as sticks. A lipid molecule with the headgroup interacting with R941 is shown in dark teal sticks (**E**).

membrane defect with lipid headgroups and water molecules located in the bilayer middle is associated with a substantial energetic cost, although this cost can be compensated for by a sufficiently hydrophobic sequence in the TM (22–24). R941 and E871 engage in stable salt-bridge interactions that can screen the charges from the hydrophobic environment of the lipid tails, requiring no headgroups to be pulled in to interact with R941. However, when stable interactions are not formed, this screening effect does not take place, and thus the membrane defect and the cone of water molecules compensate for the charges of R941 and E871. One reason for this defect forming only in the ATP-free state

could be a more polar environment surrounding E871 and R941 in the absence of ATP: here, the extracellular end of TM8 not only orients away from the central pore, but also partially rotates (with respect to the ATP-bound state) so that the side chain of Y927 points toward the hydrophobic region of the bilayer (Fig. 2; Fig. S8). This allows the Y927 side chain to interact with water molecules and lipid headgroups once the defect is formed (Fig. 2, *E* and *F*). In the ATP-bound system, on the other hand, the simulations show a persistent interaction between Y927 and S875, with Y927 prevented from interacting with water molecules, together with a more buried R941 side chain (Figs. 2 and

S8). It should be noted that the cryo-electron microscopy structures of CFTR do not provide detailed density for the side chain of E871, and thus structural artifacts due to a nonideal initial side-chain modeling can occur. However, for each ATP-free and ATP-bound simulation, we carried out independent equilibration steps to allow for the sampling of different side-chain conformations. Thus, it seems plausible that a membrane defect, although a rare event, might occur in the ATP-free state, linked to a more polar environment because of Y927 and a more exposed R941 side chain.

Combined, our simulations support the stability of the unusual unwound segment of TM8 in the ATP-bound and ATP-free state of CFTR. The simulations also highlight a pool of interactions, common to both states, between TM8 and nearby helices that prevent further folding or unfolding of TM8 and contribute to the architecture of the channel. Although at present we can only speculate on the specific role of the residues we investigated, this study supports the development of experimental hypotheses to evaluate the contribution of TM8 residues, and in particular R941 interactions with other TMs and/or lipid headgroups, to the gating mechanism of CFTR.

## SUPPORTING MATERIAL

Supporting Materials and Methods, eight figures, two tables, and three data files are available at [http://www.biophysj.org/biophysj/supplemental/S0006-3495\(18\)30300-X](http://www.biophysj.org/biophysj/supplemental/S0006-3495(18)30300-X).

## AUTHOR CONTRIBUTIONS

V.C., P.V., and D.P.T. designed the project. R.-X.G. performed the simulations and carried out the DSSP analysis. V.C. performed the remaining analyses and wrote the manuscript with P.V. and D.P.T., with contributions from R.-X.G.

## ACKNOWLEDGMENTS

We would like to thank Jue Chen, Rockefeller University, for helpful information on cryo-EM density maps.

This work was supported by the Canadian Institutes of Health Research. Additional support came from Alberta Innovates Health Solutions and Alberta Innovates Technology Futures. R.-X.G. is supported by fellowships from Alberta Innovates Health Solutions and the Canadian Institutes for Health Research (funding reference number: MFE-140949). D.P.T. holds the Alberta Innovates Technology Futures Strategic Chair in (Bio)Molecular Simulation. Simulations were run on Compute Canada machines, supported by the Canada Foundation for Innovation and partners. This work was undertaken, in part, thanks to funding from the Canada Research Chairs program. P.V. thanks the Cystic Fibrosis Trust for support.

## REFERENCES

- Rommens, J. M., M. C. Iannuzzi, ..., N. Hidaka. 1989. Identification of the cystic fibrosis gene: chromosome walking and jumping. *Science*. 245:1059–1065.
- Cheng, S. H., R. J. Gregory, ..., A. E. Smith. 1990. Defective intracellular transport and processing of CFTR is the molecular basis of most cystic fibrosis. *Cell*. 63:827–834.
- Linsdell, P. 2017. Architecture and functional properties of the CFTR channel pore. *Cell. Mol. Life Sci*. 74:67–83.
- Liu, F., Z. Zhang, L., ..., J. Chen. 2017. Molecular structure of the human CFTR ion channel. *Cell*. 169:85–95.e8.
- Zhang, Z., and J. Chen. 2016. Atomic structure of the cystic fibrosis transmembrane conductance regulator. *Cell*. 167:1586–1597.e9.
- Zhang, Z., F. Liu, and J. Chen. 2017. Conformational changes of CFTR upon phosphorylation and ATP binding. *Cell*. 170:483–491.e8.
- Tordai, H., I. Leveles, and T. Hegedűs. 2017. Molecular dynamics of the cryo-EM CFTR structure. *Biochem. Biophys. Res. Commun*. 491:986–993.
- Locher, K. P. 2016. Mechanistic diversity in ATP-binding cassette (ABC) transporters. *Nat. Struct. Mol. Biol*. 23:487–493.
- Wang, W., Y. El Hiani, ..., P. Linsdell. 2014. Relative contribution of different transmembrane segments to the CFTR chloride channel pore. *Pflugers Arch*. 466:477–490.
- Gao, X., Y. Bai, and T. C. Hwang. 2013. Cysteine scanning of CFTR's first transmembrane segment reveals its plausible roles in gating and permeation. *Biophys. J*. 104:786–797.
- Wang, W., Y. El Hiani, and P. Linsdell. 2011. Alignment of transmembrane regions in the cystic fibrosis transmembrane conductance regulator chloride channel pore. *J. Gen. Physiol*. 138:165–178.
- Linsdell, P. 2014. Functional architecture of the CFTR chloride channel. *Mol. Membr. Biol*. 31:1–16.
- Zhang, J., and T. C. Hwang. 2015. The fifth transmembrane segment of cystic fibrosis transmembrane conductance regulator contributes to its anion permeation pathway. *Biochemistry*. 54:3839–3850.
- Cotten, J. F., and M. J. Welsh. 1999. Cystic fibrosis-associated mutations at arginine 347 alter the pore architecture of CFTR. Evidence for disruption of a salt bridge. *J. Biol. Chem*. 274:5429–5435.
- Cui, G., C. S. Freeman, ..., N. A. McCarty. 2013. Two salt bridges differentially contribute to the maintenance of cystic fibrosis transmembrane conductance regulator (CFTR) channel function. *J. Biol. Chem*. 288:20758–20767.
- Gao, X., and T. C. Hwang. 2015. Localizing a gate in CFTR. *Proc. Natl. Acad. Sci. USA*. 112:2461–2466.
- Vergani, P., S. W. Lockless, ..., D. C. Gadsby. 2005. CFTR channel opening by ATP-driven tight dimerization of its nucleotide-binding domains. *Nature*. 433:876–880.
- Zhou, Z., S. Hu, and T. C. Hwang. 2002. Probing an open CFTR pore with organic anion blockers. *J. Gen. Physiol*. 120:647–662.
- Aleksandrov, A. A., L. Aleksandrov, and J. R. Riordan. 2002. Nucleoside triphosphate pentose ring impact on CFTR gating and hydrolysis. *FEBS Lett*. 518:183–188.
- Vergani, P., A. C. Nairn, and D. C. Gadsby. 2003. On the mechanism of MgATP-dependent gating of CFTR Cl<sup>-</sup> channels. *J. Gen. Physiol*. 121:17–36.
- Kim, C., T. Schmidt, ..., M. H. Ginsberg. 2011. Basic amino-acid side chains regulate transmembrane integrin signalling. *Nature*. 481:209–213.
- Ulmschneider, M. B., J. P. Ulmschneider, ..., S. H. White. 2017. Transmembrane helices containing a charged arginine are thermodynamically stable. *Eur. Biophys. J*. 46:627–637.
- Dorairaj, S., and T. W. Allen. 2007. On the thermodynamic stability of a charged arginine side chain in a transmembrane helix. *Proc. Natl. Acad. Sci. USA*. 104:4943–4948.
- MacCallum, J. L., W. F. Bennett, and D. P. Tieleman. 2008. Distribution of amino acids in a lipid bilayer from computer simulations. *Biophys. J*. 94:3393–3404.

**Biophysical Journal, Volume 114**

**Supplemental Information**

**Structure of Transmembrane Helix 8 and Possible Membrane Defects in  
CFTR**

**Valentina Corradi, Ruo-Xu Gu, Paola Vergani, and D. Peter Tieleman**

# Structure of transmembrane helix 8 and possible membrane defects in CFTR

V. Corradi, R.-X. Gu, P. Vergani, D.P. Tieleman

## SUPPLEMENTAL MATERIAL

### METHODS

The structures of both the ATP-free (PDB ID: 5TSI) (1) and ATP-bound (PDB ID: 5W81) (2) zebrafish CFTR were used for MD simulations. Each protein system was inserted in a POPC bilayer using the `g_membed` tool (3,4), and solvated using the TIP3P water model (5). 0.15 M NaCl, to mimic the physiological ion strength, and counterions to neutralize the system were added. Each simulation system (ca. 13 nm x 13 nm x 16 nm in x, y, and z) contained 1 protein molecule, ~500 lipids, ~60000 waters, and ~500 ions in total. Simulation of the ATP-bound state also contained 2 ATP molecules and 2 Mg<sup>2+</sup> atoms. Due to missing extracellular and intracellular residues in the structure, charged termini were used for residues at the break points, as well as the residues at the N- and C-terminal of the protein. Missing residue sidechains in the ATP-bound system were added using PyMol (The PyMOL Molecular Graphics System, Version 2.0 Schrödinger, LLC). These residues were His114, Glu115, Pro116, Glu117, Arg118, Val1127, Thr1129, Asn1130, Gln1131, Asp1132, Lys1133, Pro1134, and Gly1135.

Molecular dynamics (MD) simulations were conducted using the GROMACS v. 4.6.5 package (6,7), with an integration timestep of 2 fs, using AMBER99SB-ILDN (8) and Slipids force fields (9,10) for the protein and lipids, respectively. The parameters from (11) were used for the ATP molecules. The temperature was maintained at 310 K using the *v*-rescale algorithm (12) and a relaxation time of 0.5 ps. Semi-isotropic pressure coupling and Parrinello-Rahman algorithm (13,14), with a relaxation time of 10.0 ps, were applied to maintain the pressure at 1 bar. The LINCS algorithm (15) was employed to constrain all bonds. A cutoff of 1.0 nm was used for van der Waals interactions and electrostatic interactions. The long-range electrostatic interactions were treated using the Particle Mesh Ewald (PME) algorithm (16,17). For each simulation, prior to the production run, we performed a 20 ns equilibrium simulation with position restraints applied on all the protein non-hydrogen atoms (using a force constant of 1000 kJ/(mol nm<sup>2</sup>), followed by 5 ns simulation with position restraints applied only on the backbone atoms, and 5 additional ns with position restraints on the  $\alpha$ -carbons only. The simulations carried out in this study are summarized in Table S1.

### ANALYSES

The secondary structure analysis was carried out with the GROMACS v. 4.6.5 `do_dssp` tool, which uses DSSP libraries (18,19). RMSD, distances, minimum distances and the dynamic selection of number of water molecules or phosphate atoms were computed using the corresponding GROMACS tools. The number density analysis, applied to the last 50 ns of each simulation, was carried out for water molecules using the method previously described in (20). All the voxels with a density value that is above 50% of the maximum observed density value were displayed as volume maps with PyMOL (The PyMOL Molecular Graphics System, Version 1.7 Schrödinger, LLC). The figures were generated with PyMOL or VMD (21). Matplotlib libraries were used for plotting (22).

**SI TABLES**

**Table S1.** Simulations performed in this study. For each simulation, the equilibration steps described in the Methods section above were carried out independently, to ensure a greater degree of independence of the simulations and increase the degree of sampling.

<b>System</b>	<b>Simulation length</b>	<b>Simulation</b>
<b>ATP-free</b>	1 $\mu$ s	Run 1
	500 ns	Run 1
		Run 2
		Run 3
		Run 4
<b>ATP-bound</b>	1 $\mu$ s	Run 1
	500 ns	Run 1

**Table S2.** Human CFTR (hCFTR) residues corresponding to the zebrafish CFTR (zCFTR) residues pairs analyzed in this work.

<b>Residue pairs</b>			
<b>zCFTR</b>	<b>hCFTR</b>	<b>zCFTR</b>	<b>hCFTR</b>
Y925	Y917	S342	S341
Y927	Y919	S877	S875
E932	D924	R348	R347
S933	T925	F312	F311
M937	M929	Y305	Y304
M937	M929	Q1004	Q996
R941	R933	E871	E873

## SUPPLEMENTAL FIGURES

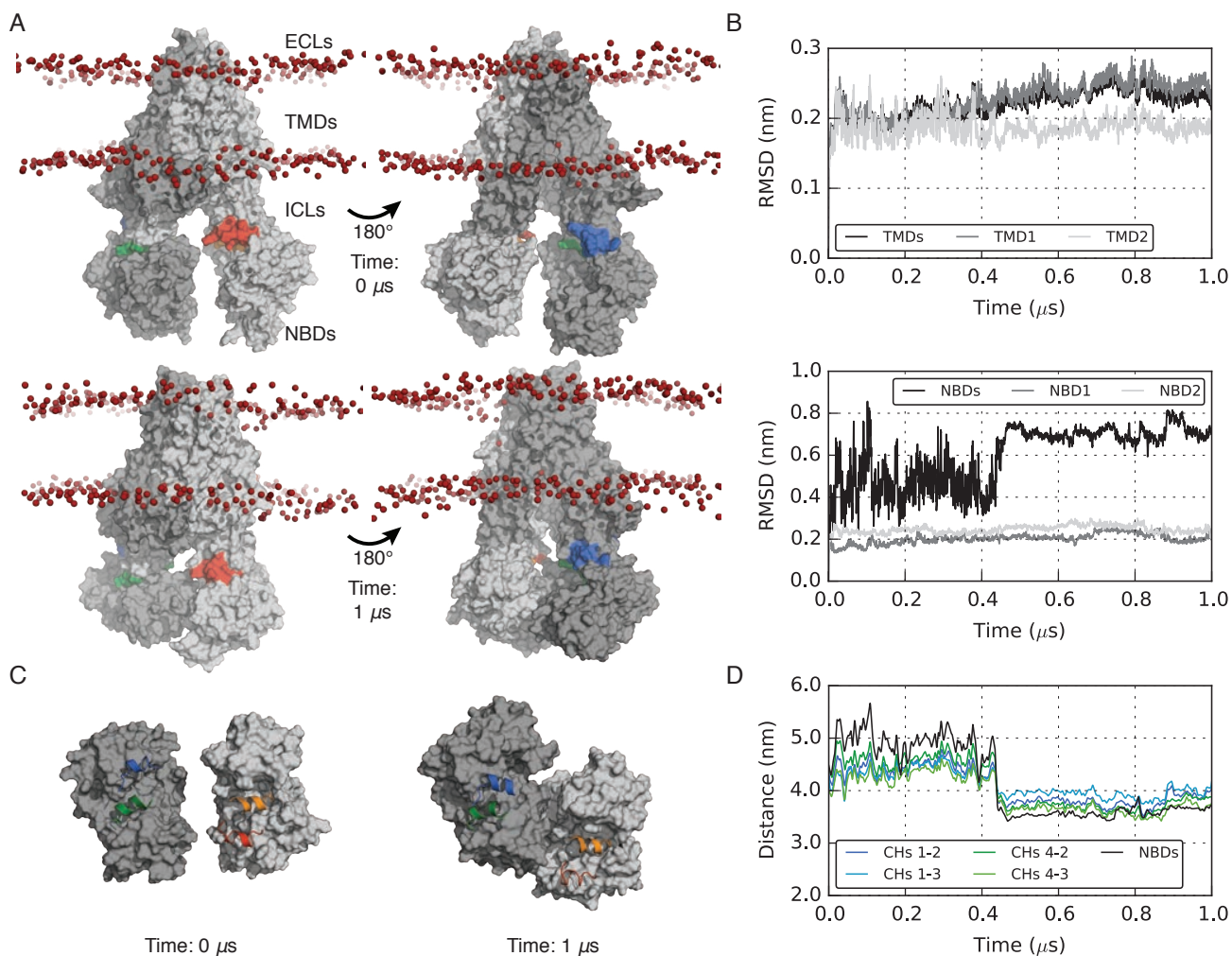


**Figure S1. Overall protein conformation of the ATP-free CFTR system.**

A. Snapshots of the simulation system taken at 0 (top panels) and 1 (bottom panels)  $\mu\text{s}$ . TMD1 and NBD1 are shown in dark gray surface, while TMD2 and NBD2 are shown in light gray surface. The residues forming the coupling helices (CHs) are colored in blue, orange, red and green for CH 1, 2, 3 and 4, respectively. The phosphate atoms of the POPC molecules are shown in dark-red spheres. B. RMSD values for the TMDs, TMD1, TMD2 (black, dark and light gray line, respectively) and the NBDs, NBD1, NBD2 (black, dark and light gray line, respectively). C. Snapshots of NBDs taken at 0 and 1  $\mu\text{s}$  to highlight distances between the CHs sampled during the simulation. Colors are as in A. D. Distances between the  $\alpha\text{C-COM}$  ( $\alpha$ -carbons center of mass) of the CHs and between NBD1-NBD2, shown as a function of time.

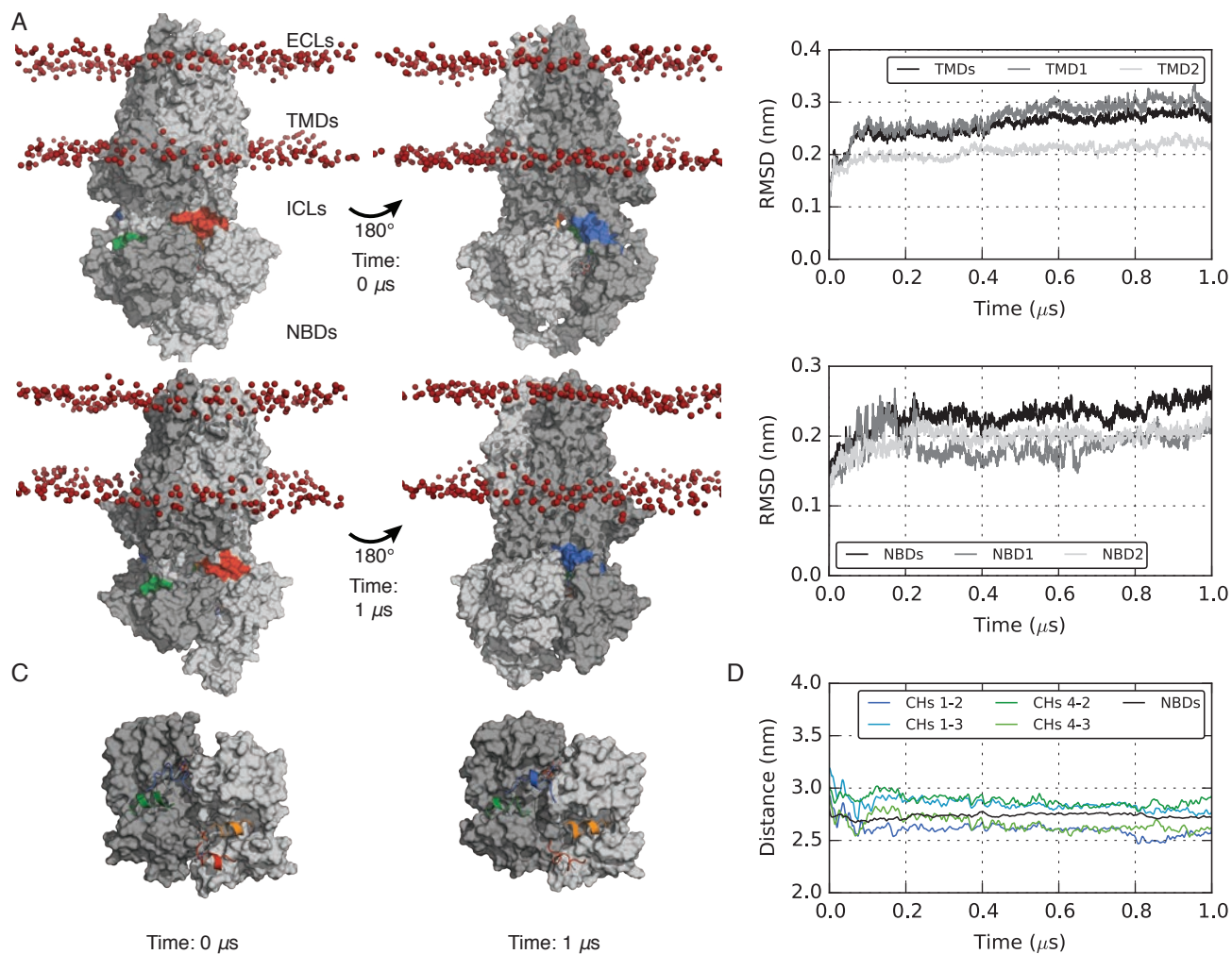


**Figure S2. Overall protein conformation of the ATP-bound CFTR system.**

A. Snapshots of the simulation system taken at 0 (top panels) and 1 (bottom panels) μs. Colour-coding as in Figure S1. C. Snapshots of NBDs taken at 0 and 1 μs. D. Distances between the  $\alpha$ C-COM ( $\alpha$ -carbons center of mass) of the coupling helices (CHs) and between NBD1-NBD2, shown as a function of time.

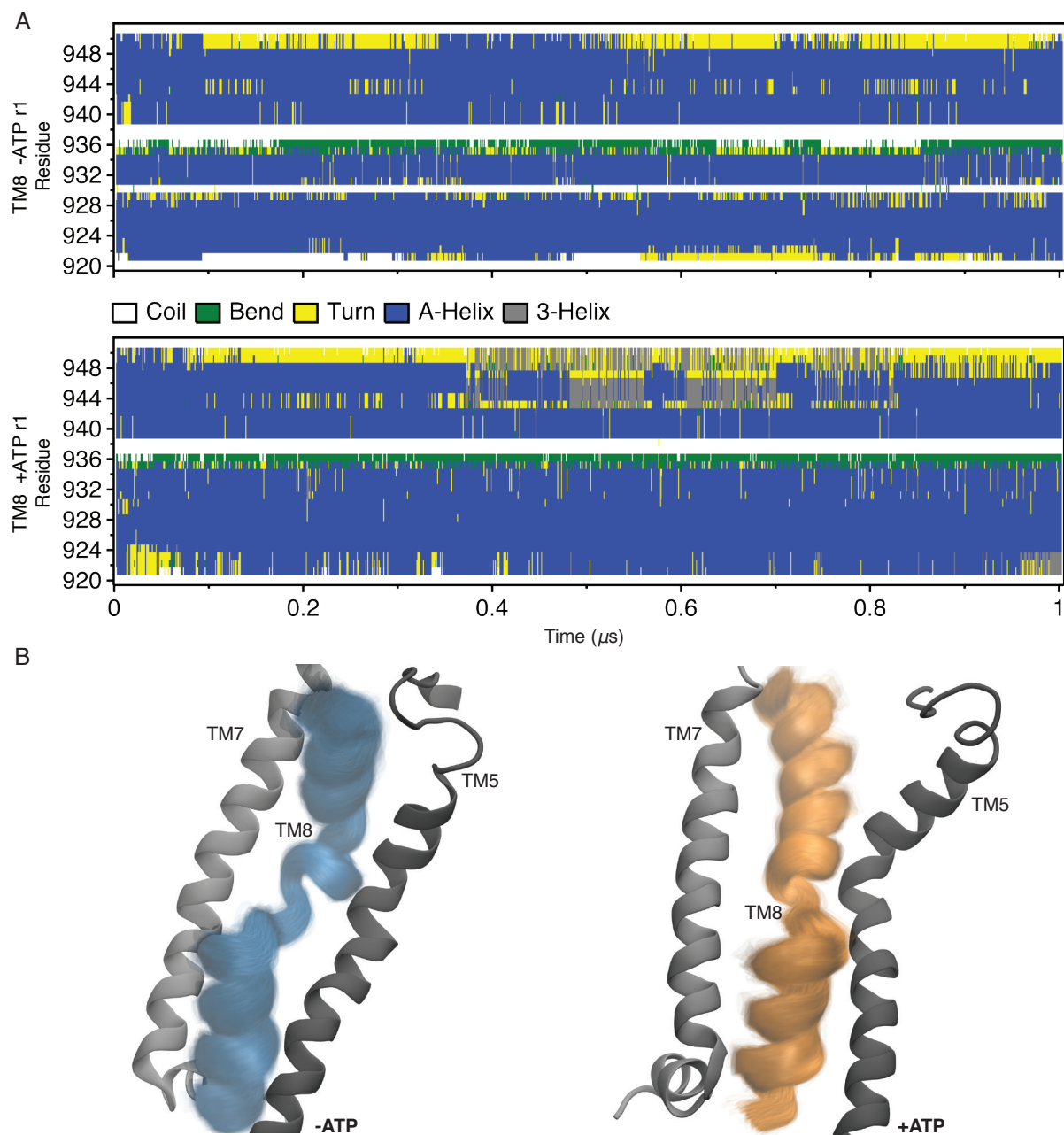


**Figure S3. Stability of the unwound segment of TM8 over the 1  $\mu$ s long simulations.**

A. The secondary structure analysis of the TM8 residues 921-951 is shown as function of time for the ATP-free (top panel, -ATP) and ATP-bound (bottom panel, +ATP) 1  $\mu$ s-long simulations. B. Superimposition of the TM8 conformations extracted every 200 ps over 1  $\mu$ s of simulation time. Each snapshot shows TM8 in transparent blue (ATP-free system) and orange (ATP-bound system) cartoons. All the snapshots were aligned to the structure extracted after 1  $\mu$ s of simulation time based on the  $\alpha$ -carbon atoms only, after progressive fitting. Shown are also TM7 and TM5 at 1  $\mu$ s of simulation time.

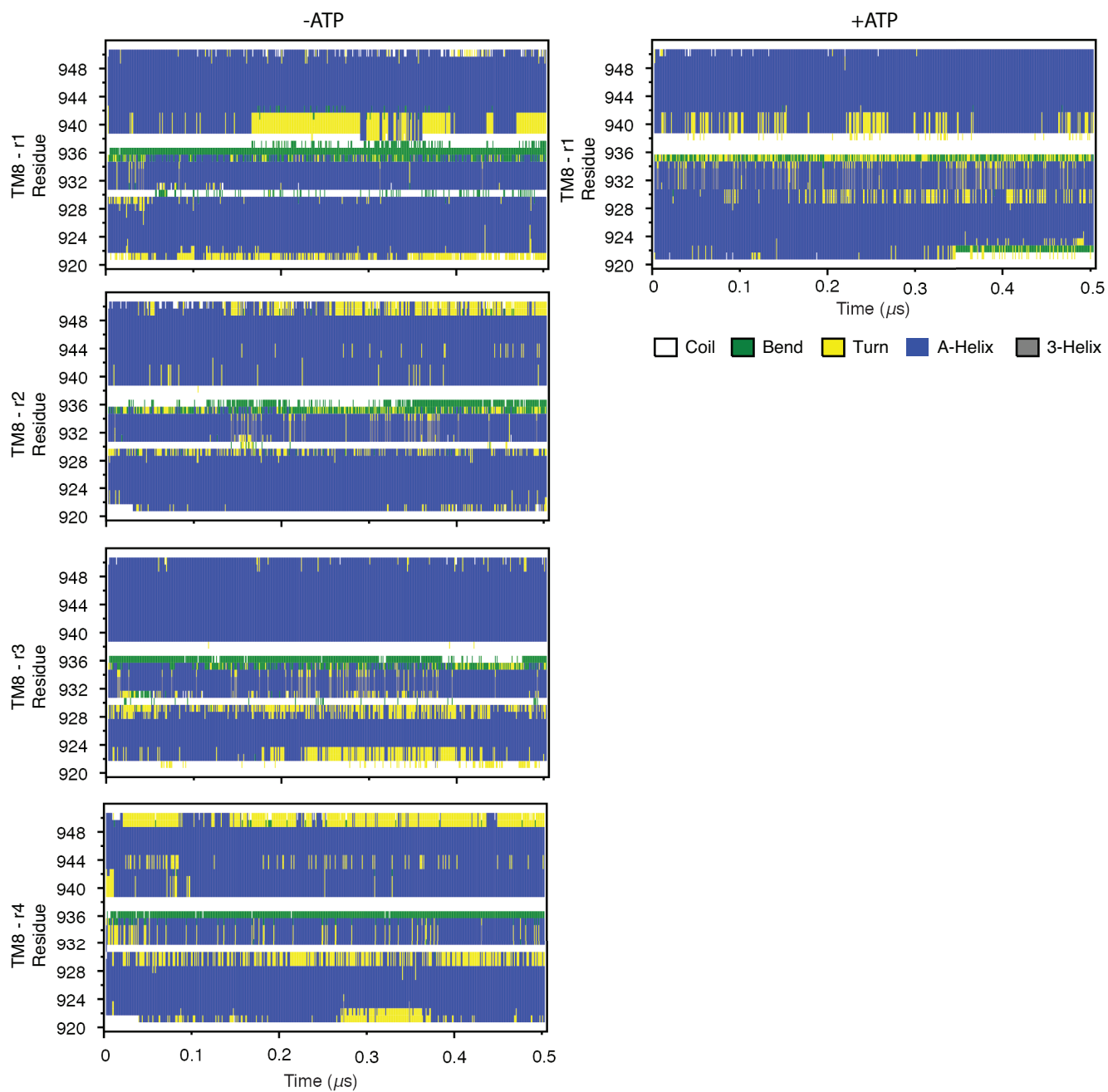


**Figure S4. Stability of the unwound segment of TM8 over the 500 ns-long simulations.**

The secondary structure of the TM8 residues 921-951 is shown as a function of time for the four 500 ns-long ATP-free (-ATP, left panels) and the 500 ns long ATP-bound (+ATP, right panel) simulations listed in Table S1.

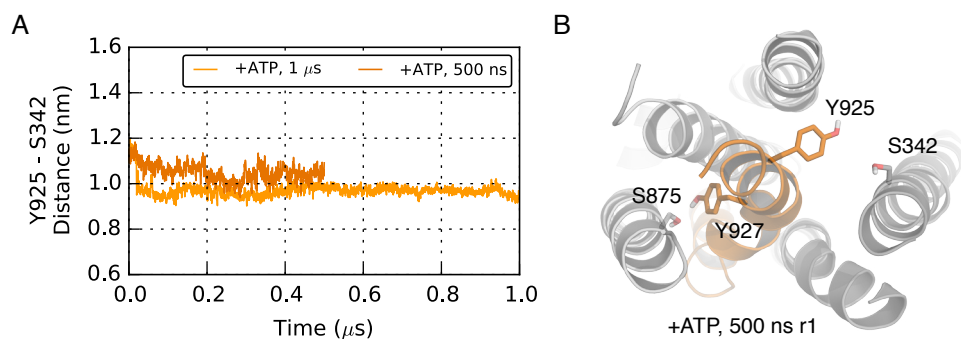


**Figure S5. Y925 - S342 distance profile in the ATP-bound (+ATP) simulations.**

A. The distance between the  $\alpha$ -carbons of Y925 and S342 is shown as a function of time for the ATP-bound 1  $\mu$ s- and 500 ns-long simulations. B. Snapshot taken at 500 ns from the 500 ns-long simulation showing the lack of hydrogen bond interaction between the side chain of Y925 and S342. The protein is viewed from the extracellular side, as in Figure 2B. Y925, S342, Y927 and S875 are shown as sticks.

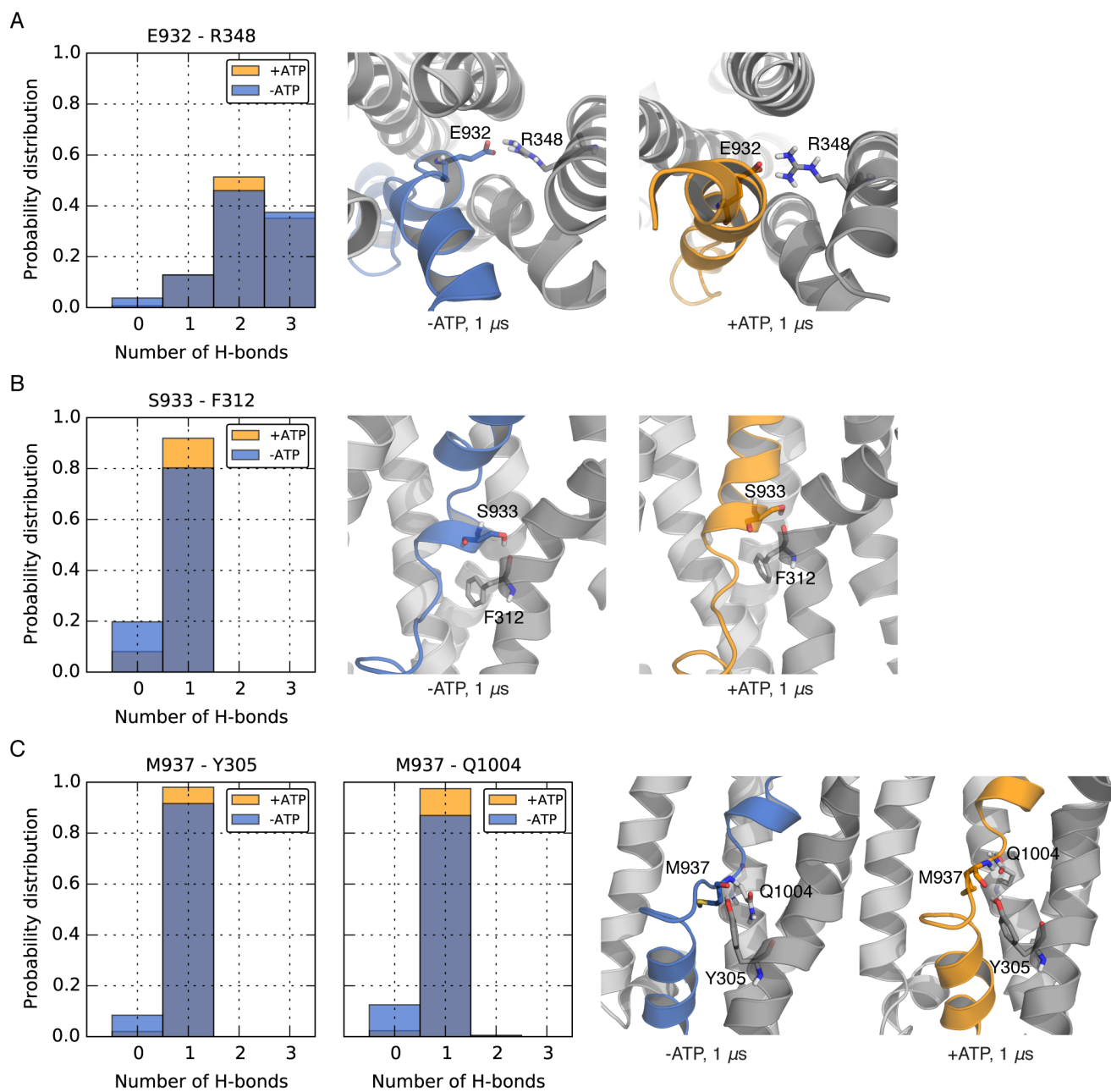


**Figure S6. Probability distribution of hydrogen bond interactions.**

A-C. The probability distribution of the number of hydrogen bonds detected between the selected residues pairs is shown in blue for the ATP-free (-ATP) simulations and in orange for the ATP-bound (+ATP) simulations. The probability distribution was calculated considering all the ATP-free or ATP-bound simulations at once. For each panel, a close-up view of the selected pairs is shown using the ATP-free and ATP-bound structures obtained after 1  $\mu$ s of simulation time. TMD1 and TMD2 are shown in dark and light gray cartoons, respectively, with TM8 highlighted in blue (-ATP) or orange (+ATP).

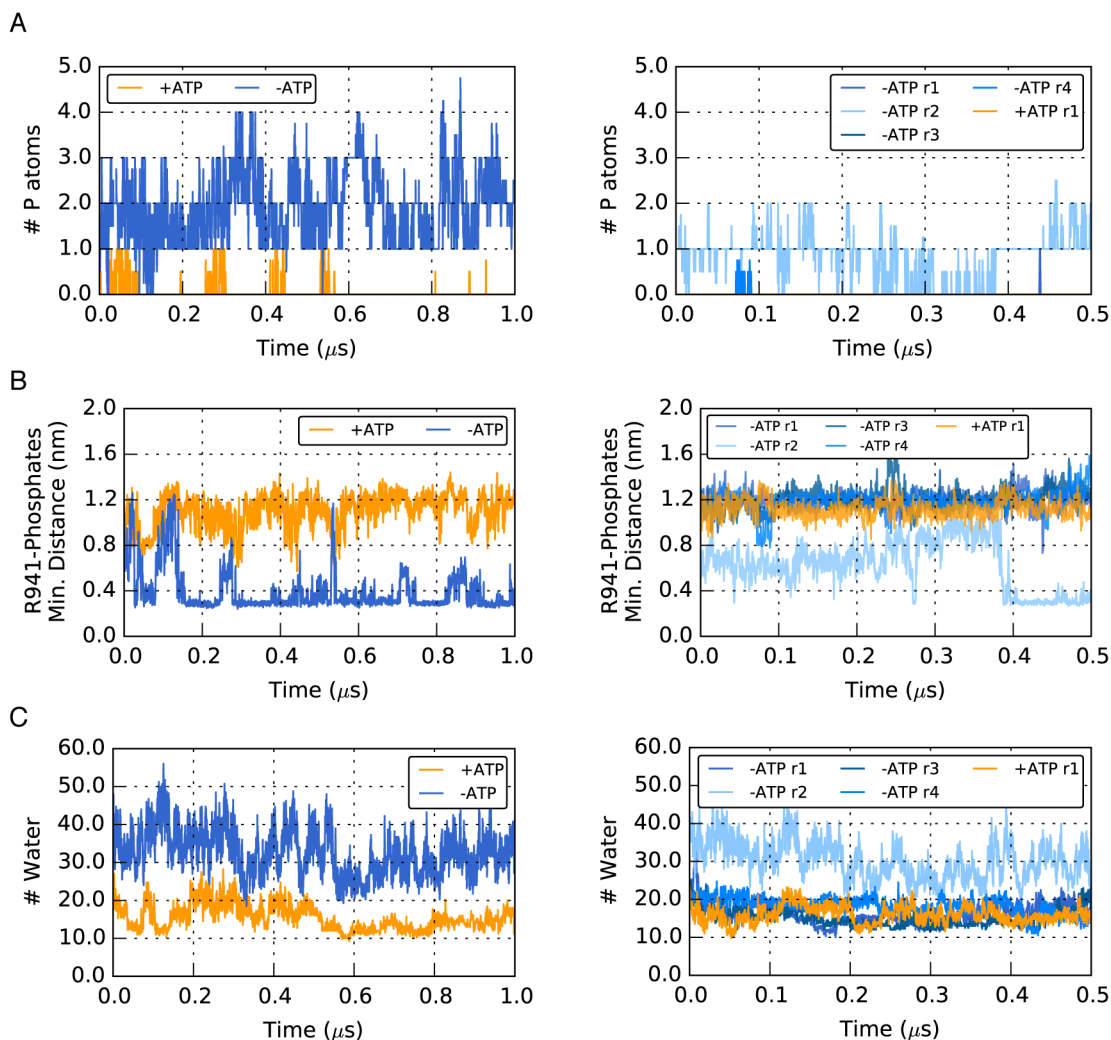


**Figure S7. Evaluation of a possible membrane and water defect around TM8.**

A. The number of lipid phosphate atoms within 8 Å of R941 and E871 is shown as function of time for the 1  $\mu$ s-long (left) and 500 ns-long (right) simulations. B. Minimum distance between R941 and lipid phosphate atoms shown as function of time for the 1  $\mu$ s long (left) and 500 ns long (right) simulations. C. Number of water molecules detected within 8 Å of R941 and E871, shown as a function of time for the 1  $\mu$ s long (left) and 500 ns long (right) simulations. The ATP-free (-ATP) and ATP-bound (+ATP) simulations are indicated in blue and orange, respectively.

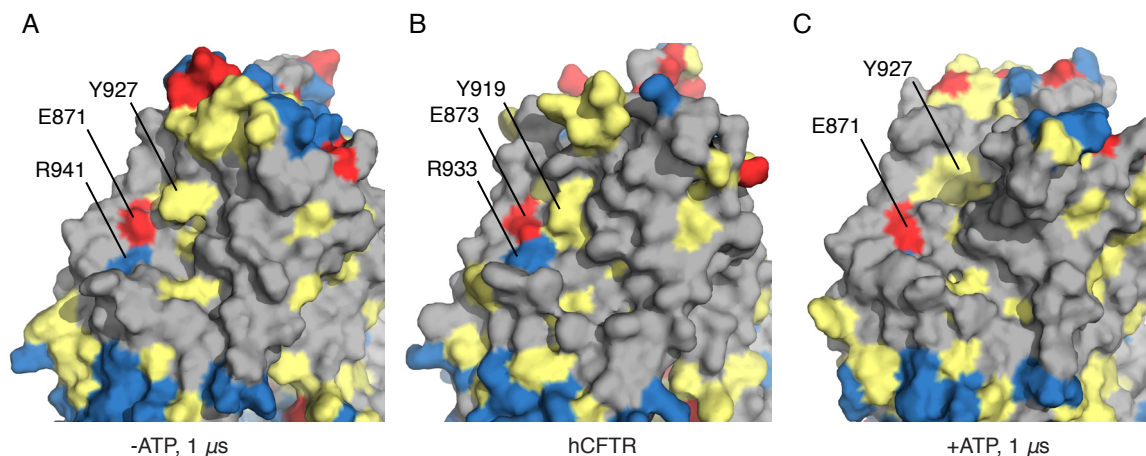


**Figure S8. Distribution of polar residues near the unwound segment of TM8 in three different experimental CFTR structures.**

Surface representation of (A) the ATP-free (-ATP) structure obtained after 1  $\mu$ s of simulation time; (B) the ATP-free, human CFTR (hCFTR) structure (PDB ID 5UAK); (C) the ATP-bound (+ATP) structure obtained after 1  $\mu$ s of simulation time. Positively charged residues are colored in blue; negatively charged residues are colored in red; polar residues such as ASN, GLN, THR, SER, CYS, TYR and TRP are colored in yellow; the remaining amino acids are colored in gray. The key residues E871, R941 (E873, R933 in human CFTR) involved in a salt bridge and/or membrane defect and Y927 (Y919 in human CFTR), providing additional possible hydrophilic interactions for water and lipid headgroups are labeled.

## REFERENCES

1. Zhang, Z. and J. Chen. 2016. Atomic Structure of the Cystic Fibrosis Transmembrane Conductance Regulator. *Cell* 167:1586-1597 e1589.
2. Zhang, Z., F. Liu, and J. Chen. 2017. Conformational Changes of CFTR upon Phosphorylation and ATP Binding. *Cell* 170:483-491.
3. Wolf, M. G., M. Hoefling, C. Aponte-Santamaria, H. Grubmuller, and G. Groenhof. 2010. *g\_membed*: Efficient Insertion of a Membrane Protein into an Equilibrated Lipid Bilayer with Minimal Perturbation. *J Comput Chem* 31:2169-2174.
4. Yesylevskyy, S. O. 2007. ProtSqueeze: Simple and effective automated tool for setting up membrane protein simulations. *Journal of Chemical Information and Modeling* 47:1986-1994.
5. Jorgensen, W. L., J. Chandrasekhar, J. D. Madura, R. W. Impey, and M. L. Klein. 1983. Comparison of Simple Potential Functions for Simulating Liquid Water. *J Chem Phys* 79:926-935.
6. Hess, B., C. Kutzner, D. van der Spoel, and E. Lindahl. 2008. GROMACS 4: Algorithms for highly efficient, load-balanced, and scalable molecular simulation. *J Chem Theory Comput* 4:435-447.
7. Pronk, S., S. Pall, R. Schulz, P. Larsson, P. Bjelkmar, R. Apostolov, M. R. Shirts, J. C. Smith, P. M. Kasson, D. van der Spoel, B. Hess, and E. Lindahl. 2013. GROMACS 4.5: a high-throughput and highly parallel open source molecular simulation toolkit. *Bioinformatics* 29:845-854.
8. Lindorff-Larsen, K., S. Piana, K. Palmo, P. Maragakis, J. L. Klepeis, R. O. Dror, and D. E. Shaw. 2010. Improved side-chain torsion potentials for the Amber ff99SB protein force field. *Proteins* 78:1950-1958.
9. Jambeck, J. P. M. and A. P. Lyubartsev. 2012. Derivation and Systematic Validation of a Refined All-Atom Force Field for Phosphatidylcholine Lipids. *J Phys Chem B* 116:3164-3179.
10. Jambeck, J. P. M. and A. P. Lyubartsev. 2012. An Extension and Further Validation of an All-Atomistic Force Field for Biological Membranes. *J Chem Theory Comput* 8:2938-2948.
11. Meagher, K. L., L. T. Redman, and H. A. Carlson. 2003. Development of polyphosphate parameters for use with the AMBER force field. *J Comput Chem* 24:1016-1025.
12. Bussi, G., D. Donadio, and M. Parrinello. 2007. Canonical sampling through velocity rescaling. *J Chem Phys* 126.
13. Nose, S. 1984. A Molecular-Dynamics Method for Simulations in the Canonical Ensemble. *Mol Phys* 52:255-268.
14. Parrinello, M. and A. Rahman. 1981. Polymorphic Transitions in Single-Crystals - a New Molecular-Dynamics Method. *J Appl Phys* 52:7182-7190.
15. Hess, B., H. Bekker, H. J. C. Berendsen, and J. G. E. M. Fraaije. 1997. LINCS: A linear constraint solver for molecular simulations. *J Comput Chem* 18:1463-1472.
16. Darden, T., D. York, and L. Pedersen. 1993. Particle Mesh Ewald - an N.Log(N) Method for Ewald Sums in Large Systems. *J Chem Phys* 98:10089-10092.
17. Essmann, U., L. Perera, M. L. Berkowitz, T. Darden, H. Lee, and L. G. Pedersen. 1995. A Smooth Particle Mesh Ewald Method. *J Chem Phys* 103:8577-8593.
18. Joosten, R. P., T. A. te Beek, E. Krieger, M. L. Hekkelman, R. W. Hooft, R. Schneider, C. Sander, and G. Vriend. 2011. A series of PDB related databases for everyday needs. *Nucleic Acids Res* 39:D411-419.
19. Kabsch, W. and C. Sander. 1983. Dictionary of protein secondary structure: pattern recognition of hydrogen-bonded and geometrical features. *Biopolymers* 22:2577-2637.
20. Mehmood, S., V. Corradi, H. G. Choudhury, R. Hussain, P. Becker, D. Axford, S. Zirah, S. Rebuffat, D. P. Tieleman, C. V. Robinson, and K. Beis. 2016. Structural and Functional Basis for Lipid Synergy on the Activity of the Antibacterial Peptide ABC Transporter McjD. *J Biol Chem* 291:21656-21668.
21. Humphrey, W., A. Dalke, and K. Schulten. 1996. VMD: visual molecular dynamics. *J Mol Graph* 14:33-38, 27-38.
22. Hunter, J. D. 2007. Matplotlib: A 2D graphics environment. *Comput Sci Eng* 9:90-95.